

Appendix A.

Supplementary material to the manuscript:

The role of crustal and eruptive processes versus source variations in controlling the oxidation state of iron in Central Andean magmas

1. Continental crust beneath the CVZ

Country Rock

The basement beneath the sampled portion of the CVZ belongs to the Paleozoic Arequipa-Antofalla terrain – a high temperature metamorphic terrain with abundant granitoid intrusions that formed in response to Paleozoic subduction (Lucassen et al., 2000; Ramos et al., 1986). In Northern Chile and Northwestern Argentina this Paleozoic metamorphic-magmatic basement is largely homogeneous and felsic in composition, consistent with the thick, weak, and felsic properties of the crust beneath the CVZ (Beck et al., 1996; Fig. A.1). Neodymium model ages of exposed Paleozoic metamorphic-magmatic basement and sediments suggest a uniform Proterozoic protolith, itself derived from intrusions and sedimentary rock (Lucassen et al., 2001).

AFC Model Parameters

Pervasive assimilation of continental crust in the Central Andean ignimbrite magmas is well established (Hildreth and Moor bath, 1988; Klerkx et al., 1977; Fig. A.1) and has been verified by detailed analysis of radiogenic isotopes (e.g. $^{87}\text{Sr}/^{86}\text{Sr}$ and $^{143}\text{Nd}/^{144}\text{Nd}$) on specific systems within the CVZ (Kay et al., 2011; Lindsay et al., 2001; Schmitt et al., 2001; Soler et al., 2007). Isotopic results indicate that the CVZ magmas are the result of mixing between a crustal endmember, mainly gneisses and plutonics that have a characteristic crustal signature of high $^{87}\text{Sr}/^{86}\text{Sr}$ and low $^{145}\text{Nd}/^{144}\text{Nd}$, and the asthenospheric mantle (low $^{87}\text{Sr}/^{86}\text{Sr}$ and high $^{145}\text{Nd}/^{144}\text{Nd}$; Fig. 2). In Figure 2, we model the amount of crustal assimilation required to produce the CVZ magmas that are targeted in this study. For our geochemical models, we use the

isotopic values of Schmitt et al. (2001) in their study of the Purico and La Pacana systems ($^{87}\text{Sr}/^{86}\text{Sr} = 0.7028$ and $^{145}\text{Nd}/^{144}\text{Nd} = 0.5130$) as the initial mantle-derived basaltic melts delivered to the lower crust of the Central Andes. The Chilean gneisses and Ordovician granitoids show a range of compositions ($^{87}\text{Sr}/^{86}\text{Sr} = 0.708$ to 0.840) but a histogram of the data suggests that the range of the assimilant is more likely between $^{87}\text{Sr}/^{86}\text{Sr} = 0.705$ and 0.725 (Fig. A.2; Lucassen et al., 2001). The partitioning of Sr and Nd elements in the magmatic systems of the Central Andes is consistent with a range in bulk partition coefficients for Sr ($D_{\text{Sr}} = 1$ to 3) and Nd ($D_{\text{Nd}} = 0.1$ to 2 ; de Silva et al., 2006; Folkes et al., 2013; Hildreth and Moorbath, 1988; Kay et al., 2010; Klerkx et al., 1977). We chose to use a bulk partition coefficient of 1 for Sr and 0.1 for Nd. We present two models (Fig. 2) that use the likely endmember bulk compositions of the crustal contaminant based on the range in Andean basement material analyzed by Lucassen et al. (2001; Fig. A.2). Geochemical modeling shows that the most primitive basaltic andesite lavas in the Central Andes require at least 20 vol.% crustal assimilation, while the large-volume magmas that contain the most highly evolved chemical signatures observed in CVZ require between 40 to 100 vol.% assimilation (Fig. 2). These results are consistent with previous models that have attempted to quantify the amount of crustal assimilation in CVZ magmas (de Silva et al., 2006; Folkes et al., 2013; 2011; Kay et al., 2011; 2010; Ort et al., 1996).

2. Geochemistry of CVZ magmas

SiO₂ as a differentiation index and LLDs of CVZ magmas

All CVZ systems we investigate here show evidence for assimilation-fractional crystallization, or AFC (Fig. 2). This choice was deliberate because we have designed our study to assess the influence of AFC on magmatic $\text{Fe}^{3+}/\Sigma\text{Fe}$ ratios. Because of the AFC signature, the

liquid lines of descent for the volcanic systems are complicated. Figures A.3 and A.4 include various Harker Diagrams for the CVZ volcanoes in this work with data available in GEOROC: Lascar, Aucanquilcha, Purico, Cerro Galan, Tata Sabaya, and Tuzgle (Fig. 1). In Figures A.3 and A.4 we also include, for comparison, GEOROC data from the Parinacota system, located in the CVZ, as it represents a closed system that has experienced no detectable AFC (Wörner et al., 1988; Davidson et al., 1990; see Panel A of Fig. A.5).

First, to ensure that SiO₂ is the appropriate index of differentiation in CVZ magmas, we compare Panels A and B in Figure A.3. The LLDs are much more distinct and show less scatter using SiO₂ as an index of differentiation when compared to Mg# (the example here is TiO₂, but any major/minor could be plotted). While MgO or Mg# are common indices to use for examining LLDs at more mafic systems, MgO and Mg# become less sensitive to differentiation in more evolved systems as the mafic phases that contribute to their decrease are lost from the crystallizing assemblage. Mg# can also be complicated as an index in more evolved magmas as Fe-rich phases (e.g., Fe-Ti oxides) saturate and fractionate. In addition, *f*O₂ variations will disrupt the expected systematics of Mg# (i.e., calculating Mg# using total Fe, introduces error because only Fe²⁺ is relevant in the olivine-melt equilibrium). This is particularly important for magmas that may have emerged from the mantle with an oxidized signature, because true Mg# (accounting for Fe³⁺) will be significantly higher than Mg# calculated using total iron. In this respect, SiO₂ may serve as a more robust index of differentiation than Mg#. Primary magmatic SiO₂ contents of arc magmas have been shown to vary due to melting of young subducted lithosphere (e.g., in the trans-Mexican volcanic belt; Straub et al., 2013) or due to unusual conditions in the mantle wedge (e.g., Mt. Shasta in California, Grove et al., 2003), but the

>40Ma age of the subducting plate beneath the CVZ (Norabuena et al., 1999) precludes this as a major factor in this region.

Second, we demonstrate that LLDs at most CVZ volcanoes show remarkably little scatter despite the pervasive influence of AFC, and that, among the volcanoes considered in this study, the LLDs are extremely similar (Panel B in Fig. A.3 and Fig. A.4). These Harker Diagrams also reinforce the utility of SiO₂ as a robust proxy for differentiation in these systems and highlights why Mg# is inappropriate.

3. Samples

We collected basaltic andesites from monogenetic, minor mafic centers behind the volcanic front in Bolivia (Cerro Luntapa, Quillacas; Figs. 1 and 2, Table 1; Table A.1). These lavas are typically small-volume and non-porphyritic (aphyric scoria to 5% crystals) with plagioclase, pyroxene, and rare olivine microphenocrysts (Davidson and de Silva, 1995). With low SiO₂ and ⁸⁷Sr/⁸⁶Sr (Table 1, Fig. 2), these samples represent the least crustally contaminated magmas in the CVZ.

We also included basaltic andesite to andesite lavas from CVZ composite volcanoes. We sampled a basaltic andesite lava from the polygenetic composite volcano of Tata Sabaya. Additional andesites include two fresh lavas erupted during the middle stages of the 11 million-year history of the Aucanquilcha Volcanic Center (AP0729, Gordo-Rojo, 4.5 Ma; AP0736, Polan-Central Manos, 3.5 Ma; Walker et al., 2013). In addition, we sampled fresh andesite lava from La Poruna, a small volume (area of 12 km² and a volume of 0.3 km³) parasitic scoria cone to San Pedro volcano in Chile (Francis et al., 1974). We also collected two andesites from the pumice that erupted in the April 1993 explosive eruption of Lascar volcano. The Lascar

pyroclastic flow deposits contain two kinds of andesite pumice, both of which were sampled: white pumice (sample 09009) with visible zonation from a white quenched rim (09009_1) to a reddish core (09009_3), and grey, dense, unaltered, more mafic andesite scoria clasts (sample 09010) (Gardeweg et al., 1998). In addition, we included a fresh basaltic andesite lava erupted in the older Soncor eruption (Gardeweg et al., 1998). Lastly, we sampled fresh andesite lava erupted from the Young Flow from Tuzgle, a Quaternary volcano unique to this sample set due to its offset location ~275 km east of the main arc front (Coira and Kay, 1993). Andesite lavas from the Young Flow show strong evidence for substantial magma mixing between upper crustal contaminants and mafic magmas that were fractionating mafic phases at high pressure (Coira and Kay, 1993).

We also sampled dacite to rhyolite pumice and lavas from the calderas of the Altiplano Puna Volcanic Complex (APVC), and the Cerro Galan caldera complex. The APVC is a Neogene ignimbrite province with a total erupted volume of >15,000 km³ (de Silva and Gosnold, 2007; Lucassen et al., 2001). Magmas associated with the APVC are “monotonous intermediates” (Hildreth and Moorbath, 1988) and have high crustal affinities owing to significant melt generation and mixing in the extremely thick (~80 km; Fig. 1) continental crust (de Silva, 1989; Folkes et al., 2011; Ort et al., 1996). Within the APVC, we focused on the Guacha caldera located in SW Bolivia that erupted the Tara deposits, including a plinian fallout pumice and a large volume (800 km³ DRE) ignimbrite (3.49 ± 0.01 Ma; Salisbury et al., 2011). We also included a fallout pumice sample erupted from Cerro Purico Volcanic Complex in NW Chile (0.98 ± 0.03 Ma). Lastly, we sampled rhyodacitic lavas and ignimbrites from Cerro Galan in NW Argentina that erupted immediately following the climactic, caldera-forming eruption (Folkes et al., 2011). Cerro Galan, a large ignimbrite forming caldera center in NW Argentina was active

from 5.6 to 2 Ma, during which it erupted >1,200 km³ DRE of calc-alkaline, high-K rhyodacitic magmas (Folkes et al., 2011). All samples from Cerro Galan show signs of surface alteration except sample CG11D2, which is black, fresh, glassy lava. In the case of the silicic samples collected from the APVC and Cerro Galan, >70% of the mass derives from crustal contamination (assimilated continental crust; Fig. 2).

4. Statistical analysis of sub-sampling magmas in the CVZ

We designed this study to test the effects of differentiation on fO_2 and thus looked for systems that spanned a range in $^{87}\text{Sr}/^{86}\text{Sr}$ and SiO_2 . We looked for samples from individual CVZ volcanoes that had $^{87}\text{Sr}/^{86}\text{Sr}$ isotopic ratios reported in the literature. For some systems that did not have previously analyzed $^{87}\text{Sr}/^{86}\text{Sr}$ ratios, but filled gaps in the range of SiO_2 , we acquired isotopic data (see Table 1). Ideally, we would have collected wet chemistry data on multiple samples from each volcano that span a large range in SiO_2 , but for the purposes of this study, we focused on the samples with $^{87}\text{Sr}/^{86}\text{Sr}$ data because assessing the impact of crustal contamination was our top priority.

It is reasonable to ask whether the choice of few, or even one, sample from each volcano would result in no correlation between $\text{Fe}^{3+}/\Sigma\text{Fe}$ ratios and indices of differentiation in the global data set, but would miss correlations within each volcanic system. To test this possibility, we used the GEOROC datasets described above for the minor element TiO_2 , which we know correlates with SiO_2 within each volcano's dataset. First, we plotted data from our specific samples on a compilation of CVZ data (Panel C in Fig. A.3). The compiled CVZ data show a general trend of increasing SiO_2 with decreasing TiO_2 and that trend is apparent in our sample suite. We then performed the same test for several trace elements (Ba, Nb, La, etc.) and show

representative results for La in Panel D in Fig A.3. We would not necessarily expect trace element concentrations to correlate with SiO₂, as trace elements can be affected by the crystallization of accessory phases and AFC processes. As found with TiO₂, the GEOROC dataset and our sample suite recover the same relationship (in this case, no correlation). These simple examples demonstrate that we expect single samples from individual volcanoes to collectively capture a comparable trend to that defined by all samples from all volcanoes.

Second, we ran a statistical test in which we assigned each sample in the GEOROC data set from a volcano a random number using the random number generator function in MS Excel, and set a numerical criterion for selection of a random sample from each volcano (we selected the lowest random number). We plotted the TiO₂-SiO₂ concentration pair for each randomly selected sample from each volcano as a group (Fig. A.6). We performed this exercise ten times and found that the random samples define linear trends similar to the trend we observe in the compiled CVZ data (Panel B in Fig. A.3). We therefore show that if correlations between SiO₂ and Fe³⁺/ΣFe ratios or between ⁸⁷Sr/⁸⁶Sr isotopic ratios and Fe³⁺/ΣFe ratios existed within each volcano's magmas, we expect that our data set would have captured this variation in Figures 4 and 5 of the main text.

5. Analytical Methods

Whole Rock Major Element and Isotope Analysis

Major element compositions of bulk samples new to this study were determined by X-Ray Fluorescence (XRF; Thermo ARL) following the procedures of Johnson et al. (1999) at the Washington State University GeoAnalytical Lab. In all other cases, we report the published values (FeO*; Table 2). Whole rock powders of all samples were analyzed for Sr isotopes

($^{87}\text{Sr}/^{86}\text{Sr}$) at New Mexico State University using thermal ionization mass spectrometry (TIMS). Elemental separation was done in 20 ml quartz columns containing cation exchange resin and elution medium of 2.5 N hydrochloric acid. Samples were pipetted onto the columns after being dissolved in 0.5 ml 2.5 N HCL. After samples were loaded, 2.5 N HCL was added onto the exchange columns in steps. Strontium was collected during the final 6 ml step. The strontium was placed onto a hot plate until all aqueous components were completely evaporated. The strontium samples were loaded onto rhenium filaments on either Cathodian beams (single filament only) or on the side filament of a trip filament assembly. Strontium samples were dissolved in 5% nitric acid and loaded on Cathodian beads with 3 drops of TaO_2 solution and 1 drop of 5% phosphoric acid. Strontium samples were analyzed on a VG Sector 30 mass spectrometer. Strontium samples were analyzed with strontium mass 88 at a minimum intensity at 3×10^{-11} amperes. Reproducibility of $^{87}\text{Sr}/^{86}\text{Sr}$ are within ± 0.000025 . See Ramos (1992) for additional details.

Whole Rock Wet chemistry

For $\text{Fe}^{3+}/\Sigma\text{Fe}$ determinations by wet chemistry (microcolorimetry) we powdered and prepared all whole rock samples using a steel jaw crusher and ceramic ball mill at the Smithsonian, National Museum of Natural History (NMNH). We followed the analytical methods of Carmichael (2014), the same as applied by Crabtree and Lange (2012) and Cottrell and Kelley (2011). Three USGS powdered rock standards (BCR-1, QLO-1a, and BIR-1a) were run in duplicate in each analytical session. Analyses of these USGS standards were within 0.28 wt.% FeO of the certified FeO contents (Table 3).

Electron Microprobe

Polished thin sections were made at the Smithsonian Institution, NMNH from all samples included in this study. Thin sections were subjected to petrological examination and those that contained titanomagnetite and ilmenite grains were selected for analysis. Major element compositions of coexisting titanomagnetite and ilmenite grains in thin section were determined using the JEOL-8900 electron microprobe at the Smithsonian Institution. Major element abundances were measured using a 15 keV accelerating potential, a 10 nA beam current, and a focused beam. Count times on peak and background ranged between 10-20 sec. We used the following Smithsonian, NMNH primary standards: ilmenite for Fe and Ti; kakanui hornblende for Na, Ca and Si; chromite for Al, Cr, and Mg; manganese for Mn; vanadinite for V. As secondary standards we used magnetite, ilmenite and chromite. We analyzed touching Fe-Ti oxide pairs when available but treated all grains as individual ilmenite and magnetite analyses to process all possible pairs (Table A.2). We avoided samples that showed signs of exsolution, except for the four post-collapse samples erupted at Cerro Galan, which we included to quantify the effects of mineral texture and post-emplacement alteration on calculated fO_2 (Table A.2). We report the average composition of titanomagnetite and ilmenite for each sample in the Supplementary material (Table A.2). Following Bacon and Hirschmann (1988), we screened for Mg-Mn exchange equilibrium using plots of $\log(X_{Mg}/X_{Mn})^{\text{magnetite}}$ versus $\log(X_{Mg}/X_{Mn})^{\text{ilmenite}}$ for all possible magnetite-ilmenite pairs in each sample (Fig. A.9).

μ -XANES

Fe K-edge X-ray absorption near-edge structure (XANES) was used to determine direct, *in situ* $Fe^{3+}/\Sigma Fe$ in homogenous, glassy, naturally quenched, crystal-free quartz-hosted melt

inclusions. Initially, tephra (pumice and scoria) were crushed and sieved and quartz and olivine were separated. Quartz and olivine melt inclusions were targeted due to their strong mineral structure, absence of cleavage, and resilience to post-entrapment modification by diffusive exchange and degassing. Inclusions in quartz in particular should be resilient to post-entrapment modification to the ratio of $\text{Fe}^{3+}/\Sigma\text{Fe}$ due to iron's incompatibility in quartz. Moreover, the $\text{Fe}^{3+}/\Sigma\text{Fe}$ ratios of glasses provide the best proxy for $f\text{O}_2$ because the oxidation state of iron in melt is not subject to crystal chemical constraints. Crystals were mounted in epoxy, double-side polished to a thickness of $<100\mu\text{m}$, and photographed in reflected, plane-polarized, and cross-polarized light to ensure a crystal-free path for infrared and X-ray microbeams.

Glassy melt inclusions were analyzed by collecting three Fe K-edge XANES spectra per sample, each on an independent $9\times 5\mu\text{m}$ spot, at station X26A at the National Synchrotron Light Source (NSLS), Brookhaven National Laboratory (BNL). Spectral collection and fitting details are given in full in Cottrell et al. (2009). XANES spectroscopy yields $\text{Fe}^{3+}/\Sigma\text{Fe}$ ratios directly and is independent of whole rock FeO^* measurements. The $\text{Fe}^{3+}/\Sigma\text{Fe}$ ratios of rhyolite melt inclusion glasses were quantified by referencing the drift-corrected centroid to a calibration curve constructed from experimental rhyolitic glasses with known $\text{Fe}^{3+}/\Sigma\text{Fe}$ ratios.

Energy selection was achieved with a silicon (311) channel-cut monochromator. Spectra were recorded in fluorescence mode from 7020-7229 eV. We calculated the centroid (area-weighted average energy) of the pre-edge $1s \rightarrow 3d$ crystal field transition multiplet (7110-7118 eV). We determined centroid positions by simultaneously fitting the baseline with a linear function constrained to have a positive slope and a damped harmonic oscillator (DHO) function, and the two pre-edge peaks were fit with Gaussian functions. We consistently monitored the energy reproducibility and instrumental drift throughout each session using a reference glass

(LW_0), following the procedures of Cottrell et al. (2009). The centroid energy of sample LW_0 has been defined (7112.30), and we modeled the energy drift as a linear function between each analysis of LW_0. Importantly, we use the relative shift in the centroid between known standards acquired in each beam session to quantify Fe oxidation state. The analytical precision of the centroid, determined empirically on replicate analyses of individual glasses, is 0.008 ± 0.005 eV.

6. Fe-Ti oxide geo-thermometry and oxygen-barometry using Ghiorso and Evans (2008)

Using the calibration of Ghiorso and Evans (2008), magmatic temperatures show a large range (675 to 940 °C) for all samples. The average two-sigma standard deviation in calculated temperature is within $\pm 19^\circ\text{C}$ (Fig. A.12). Pre-eruptive ΔNNO values range from +0.7 to +1.7 (Table A.2). As stated by Ghiorso and Evans (2008), at high oxygen fugacity ($\Delta\text{NNO} +1$), calculated temperatures can be in error by as much as 100 °C because temperature estimates are highly sensitive to analytical error and minor phases in the oxides. Therefore, actual temperatures likely lie somewhere between the estimates from Anderson and Lindsley (1988) and Ghiorso and Evans (2008). When oxides are treated as individual grains and all possible pairs are considered for each sample, the average difference in calculated temperatures using the two calibrations is 73°C, with neither oxybarometer yielding consistently higher or lower temperatures (Fig. A.12). The offset in temperature relates to an average difference in wt.% FeO of 0.52% (min = 0.28% and max = 0.86%), which only relates to a 0.22 average difference in ΔNNO .

7. Possible effects of magma dynamics on Fe-Ti oxides

In an evaluation of Table 3 in which we compare wt.% FeO (Fe^{2+}) from bulk rock and Fe-Ti oxides, in most cases the variation in ΔNNO from Fe-Ti oxides relates to small variations in

wt.% FeO, even for those samples that show significant alteration (1σ standard deviation in wt.% FeO is <0.20 wt.%, also shown by Crabtree & Lange (2012) for samples from Western Mexico; Table 3). Fe-Ti oxides from Tuzgle and Aucanquilcha, however, are unique in that they have a larger 1σ standard deviation in wt.% FeO when converted from ΔNNO (0.48 and 0.42 wt.%, respectively; Table 3) and show a relatively large deviation between the pre- and post-eruptive FeO concentrations (0.47 and 1.71 wt.%, respectively; Table 3), and therefore, in $\text{Fe}^{3+}/\Sigma\text{Fe}$ ratios between the bulk and Fe-Ti oxide data. This discrepancy may be due to pre-eruptive magma dynamics. At Tuzgle, for example, the deviation of 0.47% can be attributed to the variation in the Fe-Ti oxides; there is strong evidence for magma mixing between upper crustal contaminants and mafic magmas at Tuzgle, such as coexisting quartz and olivine, that may juxtapose diverse Fe-Ti oxide populations (Coira and Kay, 1993). Because samples from Aucanquilcha and Tuzgle are black, fresh, glassy, aphyric samples we have no reason to exclude whole rock data collected from these samples when interpreting our results.

8. Extended discussion on ‘gas buffering’ and the effect of S degassing and magma hydration on magmatic $f\text{O}_2$

Gas Buffering

Matthews et al., (1994) noted that sparse Fe-Ti oxide data from Lascar Volcano plotted parallel to curves of constant $\text{SO}_2/\text{H}_2\text{S}$ ratio, which lie oblique to the solid buffer curves (e.g., NNO) on $\log f\text{O}_2$ -T plots (Matthews et al., 1994; Figures 4 and 6). To explain this, Matthews et al., (1994) suggested that gas-phase equilibria might buffer magmas along these curves according to Eq. A.1 (also Eq. 1 in Matthews et al., 1994):



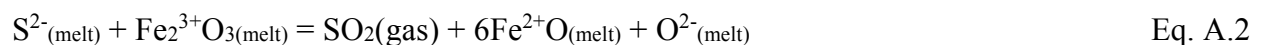
The original data that inspired the Matthews et al., (1994) model has since been supplanted by a more expansive dataset by de Hoog et al., (2004) who show that Fe-Ti oxides from Lascar lie parallel to solid buffers, eliminating the need to call upon buffering according to equation (1). However, this idea persists (Humphreys et al., 2015), driven in part by Fe-Ti oxide data from the old Matthews et al., (1994) Lascar data and data from Pallister et al., (1996) from Pinatubo (Humphreys et al., 2015, Fig 9a). de Hoog et al. (2004) plot data from Evans and Scaillet (1999) that recalibrated the data from Pallister et al., (1996) and show that Fe-Ti oxide data from Lascar and Pinatubo both follow the solid buffer curves. Thus, the two most compelling data sets provided by Humphreys et al. (2015) to suggest buffering according to Eq. A.1 have been shown to be in error and have been updated. The authors that produced the additional Fe-Ti oxide data that plot oblique to the solid buffer curves in Humphreys et al., (2015; Fig 9a) offer compelling evidence that the Fe-Ti oxides are out of equilibrium due to pre-eruptive heating (Blundy et al., 2006; Devine et al., 2003). Thus Fe-Ti oxide data does not support the idea that ‘gas buffering’ by SO₂/H₂S equilibria buffers magmatic fO_2 at higher values with lower temperature; however, there is melt inclusion data to suggest that sulfur degassing can reduce magmas (see section 6.3.2 of the main text and the following section of the Appendix).

Some confusion may stem from the Humphreys et al., (2015) incorrect description of Eq. A.1 as a “sulphide-sulphate gas-phase reaction,” when Eq. A.1 describes sulfide-sulfite equilibria in the vapor phase. Sulfide-sulfate equilibria applies to silicate melts where S is present as S⁶⁺ or S²⁻ (e.g., Jugo et al., 2010), whereas S degasses from magmas primarily as sulfite (SO₂) with S present as S⁴⁺. The error in the text extends to Humphreys et al., (2015) Figure 9a, where the curves are incorrectly labeled as XSO₄²⁻/XS²⁻ isopleths (invoking the

pyrrhotite-anhydrite buffer, which is in fact parallel to NNO and other solid buffers) when they must actually be SO₂/H₂S vapor isopleths (as in the Matthews et al., (1994) Figures 4 and 6 referenced by Humphreys et al. (2015)), though Humphreys et al., (2015) do not give the pressure at which the isopleths were calculated.

Sulfur Degassing

Sulfur degassing (Eq. A.1) can neither explain the dataset in this contribution nor be responsible for raising magmatic Fe³⁺/ΣFe ratios in the crust. Eq. A.1 is highly sensitive to pressure and shifts to the left as pressure decreases during degassing (e.g., Matthews et al., 1994; Burgisser and Scaillet, 2007; Gaillard et al., 2011; Moussallam et al., 2014). Therefore, SO₂ degassing is increasingly favored over H₂S during magma ascent. As written by Gaillard et al., (2011) on page 230: “.... The distribution of oxygen between water and sulfur species is primarily controlled by the pressure of the degassing, and that neither the redox state of the magma source nor abundance of pre-eruptive volatiles have a significant effect”. As SO₂ dominates subaerial degassing, S degassing will reduce the magma via the following equilibrium exchange (from Moussallam et al., 2014, Eq. 11):



Kelley and Cottrell (2012) and Moussallam et al., (2014) track sulfur concentration and Fe³⁺/ΣFe ratios in melt inclusions along liquid lines of descent. Both studies find that melts trapped incrementally in olivine as S degasses become progressively more reduced (lower Fe³⁺/ΣFe ratios). These studies offer compelling observational support for the thermodynamic models referenced above. As we write in section 6.3.2 entitled “Variable degassing” of the main text (L444-446), “all existing data on natural systems suggests that S degassing leads to

reduction (e.g., Anderson and Wright, 1972; Kelley and Cottrell, 2012; Moussallam et al. 2014; Shorttle et al., 2015)” consistent with these models. Moreover, in the same section of the main text (L448-453), we apply the model of Burgisser et al. (2015) to samples in our CVZ suite and show that, in the scenarios of either open or closed system H₂O-CO₂-S degassing, the magma becomes reduced by about 1 log unit. There is no evidence from observations or models that H₂O-CO₂-S degassing can oxidize magmas (see main text for additional discussion).

Melt Hydration

Based on unbuffered disequilibrium experiments where water diffused into silicate melt, Humphreys et al., (2015) suggest that melt hydration (addition of water) can result in melt oxidation (increased Fe³⁺/ΣFe ratios). In the Humphreys et al., (2015) experiments neither $f\text{H}_2$ nor $f\text{O}_2$ was held constant, but these parameters must change during hydration according to Eq. A.3 with equilibrium constant of Eq. A.4.



$$K_{\text{eq}} = f\text{H}_2\text{O} / (f\text{H}_2 \cdot f\text{O}_2^{1/2}) \quad \text{Eq. A.4}$$

We know that H₂O addition under equilibrium conditions has no power to oxidize natural magmatic systems because H₂ cannot migrate independently/selectively through magma or wall rock (as it can across noble metal tubing). Frost and Ballhaus (1998) discuss this eloquently, and Mungall (2002) indicates quite definitively that any other conclusion “violates the second law of thermodynamics.” Experimental evidence for this position abounds (e.g., Candela, 1986) but most recently comes from the equilibrium experiments of Botcharnikov et al., (2005), who find “the presence of water as a chemical component of the melt at constant T, P, and $f\text{O}_2$ has a small or insignificant influence on the Fe³⁺/ΣFe ratios.” The Botcharnikov et al., (2005) result

is consistent with Moore et al., (1995) and Gaillard et al., (2001). (Botcharnikov et al., (2005) actually show that hydrous melts have lower $\text{Fe}^{3+}/\Sigma\text{Fe}$ ratios than anhydrous basalts (their Figure 9) and highlight the importance of composition and pressure when comparing datasets, a point we discuss further in section 6.3.2 of the main text.)

Humphreys et al., (2015) suggest that disequilibrium hydration, for example during rapid ascent, could lead to “oxidation under conditions of incomplete diffusive equilibration”, and “ $\text{Fe}^{3+}/\Sigma\text{Fe}$ heterogeneity.” Careful experimental studies of disequilibrium hydration kinetics at fixed (or controlled) $f\text{H}_2$ by Gaillard et al., (2001, 2002, 2003a) yield nuanced results that depend on melt composition and H_2 diffusivity, but all studies suggest that disequilibrium between Fe oxidation state and H might affect only the outermost centimeters of magma bodies such that the “bulk volume remains unchanged” during “crustal events” (Gaillard et al., 2003b). It is important to remember that, while ascent of a water under-saturated magma from depth does result in an increase of $a\text{H}_2\text{O}$, this can only result in an increase in $f\text{O}_2$ (increase in $\text{Fe}^{3+}/\Sigma\text{Fe}$ ratios) if $f\text{H}_2$ is held constant. In an experimental apparatus, $f\text{H}_2$ can be controlled through use of a Shaw membrane, but there is no such mechanism holding $f\text{H}_2$ constant in the crust.

In summary, we find no evidence in natural or experimental systems that there is any such process as equilibrium “ H_2O driven oxidation” – by water loss or gain. The linear correlation that has been found between melt H_2O contents and the oxidation state of basalts (e.g., Cottrell and Kelley, 2009) does not require H_2O to be the oxidizing agent. The subducting plate enters the mantle with intrinsically higher oxidation state (than MORB for example), and while it also supplies the H_2O to the sub-arc mantle, H_2O has not been shown to cause the oxidized signature of the arc melts.

9. Input parameters for equilibrium degassing model results

We used input parameters ($\text{H}_2\text{O} = 4 \text{ wt.}\%$; $\text{CO}_2 = 630 \text{ ppm}$; $f\text{O}_2 = \text{NNO}+2$; pressure = 3 to 1 kbar; temperature = 900°C at 3 kbar) constrained from melt inclusions and mineral thermobarometry from Tara pumice to inform gas-melt equilibrium models that compute melt and gas CHOS compositions as a function of pressure and temperature. Based on melt solubility calibrations and gas phase equilibria for several species of each element, open or closed system equilibrium degassing of a CHOS gas phase will lead to reduction of magmatic $f\text{O}_2$ (Burgisser and Scaillet, 2015).

10. Trace elements as indicators of mantle source conditions in the CVZ

La/Nb ratio as an indicator of source composition

Using La/Nb as a proxy for source composition, we expect that, although La and Nb concentrations may vary with differentiation (Panel B in Fig. A.5), the La/Nb ratio of the CVZ samples remains constant within each volcanic center (e.g., Elliot et al., 1997). Magmas from Tuzgle show a correlation between $^{87}\text{Sr}/^{86}\text{Sr}$ and SiO_2 , and no correlation between La and SiO_2 , consistent with the strong influence of AFC processes at Tuzgle (Panels A and B in Fig. A.5). In contrast, magmas from Parinacota show large variations in SiO_2 with little to no variation in $^{87}\text{Sr}/^{86}\text{Sr}$, and systematic variation between La and SiO_2 , indicative of closed system differentiation (Panels A and B in Fig. A.5). However, the La/Nb ratios in these two systems remain constant and distinct within each volcano across variations in SiO_2 (Panel C in Fig. A.5). This comparison highlights the value of trace element ratios over individual trace element

concentrations to compare magmatic systems, and the utility of the La/Nb ratio as a proxy for mantle source composition in the CVZ (e.g., Kay et al., 2010).

Trace element indicators of slab fluid addition

Recent data suggest that aqueous slab fluids are responsible for oxidizing the mantle wedge and resultant arc magmas (Kelley and Cottrell, 2009; Kelley and Cottrell, 2012; Brounce et al., 2014). In those studies, which focus on the Mariana Arc, the authors made use of ratios of fluid-mobile to fluid-immobile trace elements, such as Ba/La, because there is no continental crust in the Marianas and assimilation is not a significant factor in influencing the basaltic compositions studied. In the CVZ, however, it is difficult to evaluate the role of aqueous fluids in the same manner because fluid mobile elements such as Rb, Ba, Pb are enriched in the continental crust. Therefore, variable degrees of AFC will result in variable enrichments of each of these elements within the CVZ magmas, independent of fluid additions of these elements to the mantle source of the primary magmas (Davidson et al., 1991; Davidson and de Silva, 1995). We find that only La/Nb (a LREE/HFSE element ratio), which is more likely a proxy for sediment addition to the mantle wedge (and not for aqueous fluid addition), exhibits a correlation with fO_2 . We discuss this correlation in terms of slab contribution mainly via bulk addition or partial melting of subducted REE enriched sediment (see section 6.4.3 of the main text), which would drive an increase in La concentrations and therefore an increase in La/Nb ratios. We limit our interpretations to what we can infer using data from the CVZ; we are unable to assess the possibility that aqueous fluids derived from the slab are responsible for oxidizing the mantle source and resultant magmas.

Supplemental figures to accompany the manuscript:
 “Controls on the oxidation state of arc magmas in the Central Andes”

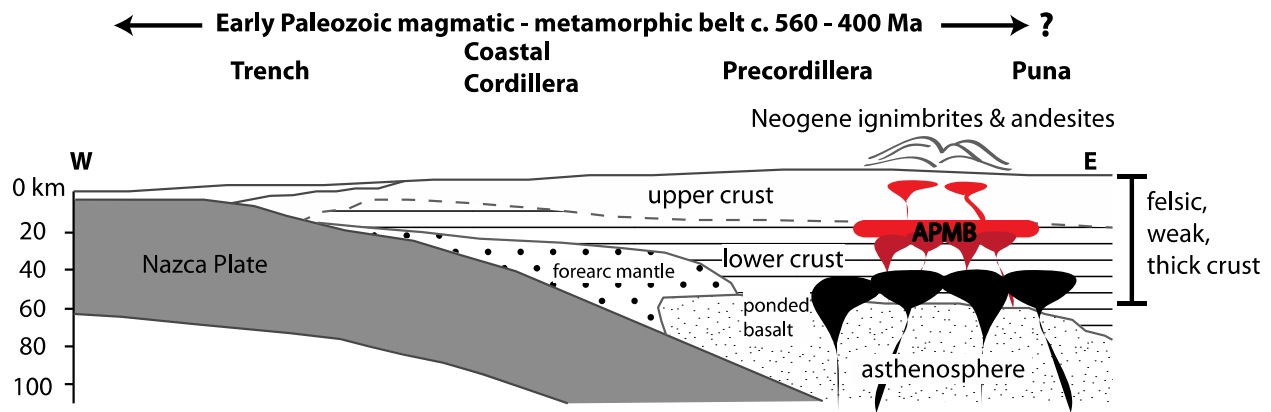


Fig. A.1 Simplified cross section modified from Lucassen et al. (2001) of the Early Paleozoic magmatic-metamorphic Central Andean basement. Roughly 70 km of thickened, felsic, weak crust comprises the basement under the CVZ. Neogene basalt flux from the mantle driven by subduction and delamination led to the accumulation of the Altiplano Puna Magma Body (APMB) and the rise of silicic magmas. Following differentiation, CVZ magmas explosively erupted from shallow magma chambers to form the CVZ ignimbrites and lavas. The interpreted magmatism is modified from de Silva et al. (2006) and represents the APVC ignimbrite “flare up” from 10 to 1 Ma.

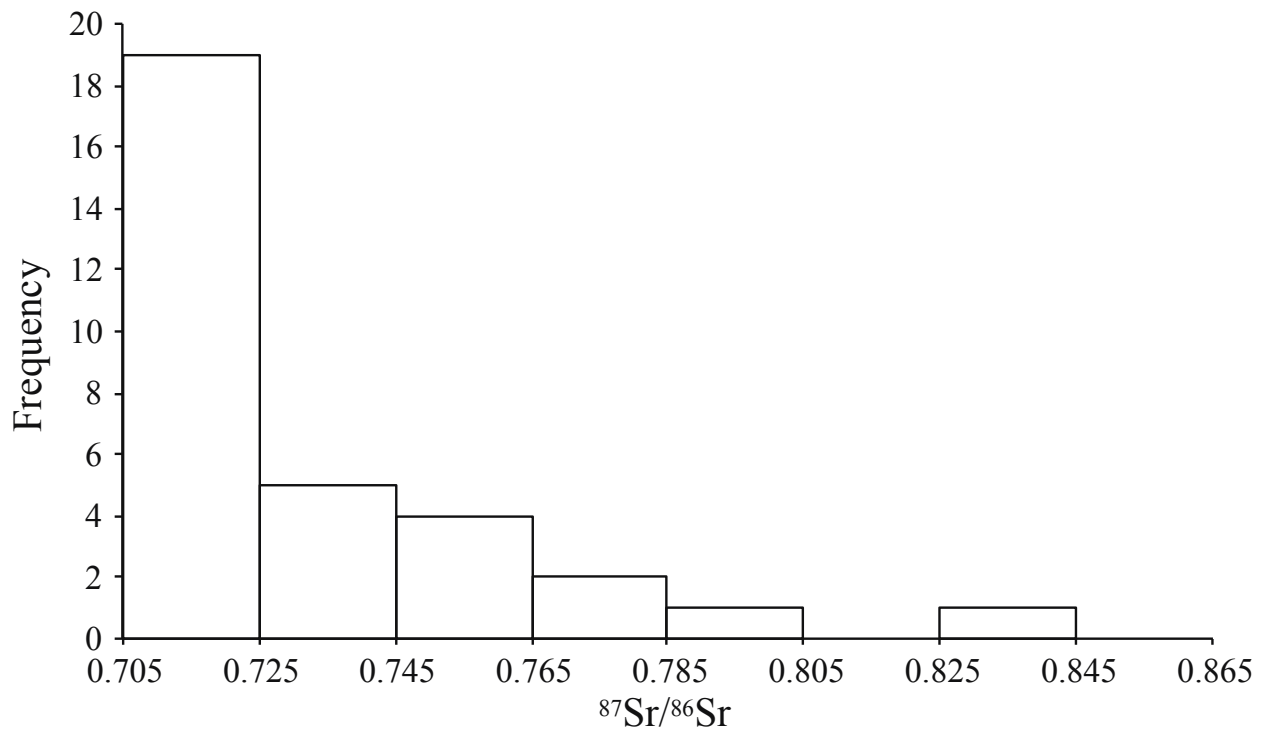


Fig. A.2 Histogram showing Andean basement isotopic compositions that are the likely assimilants for CVZ magmas from Lucassen et al. (2001).

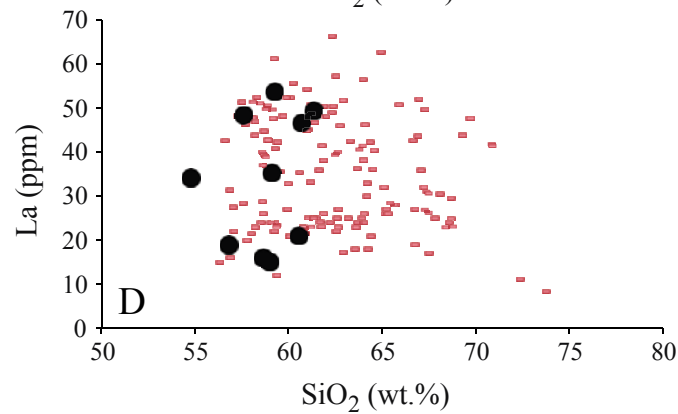
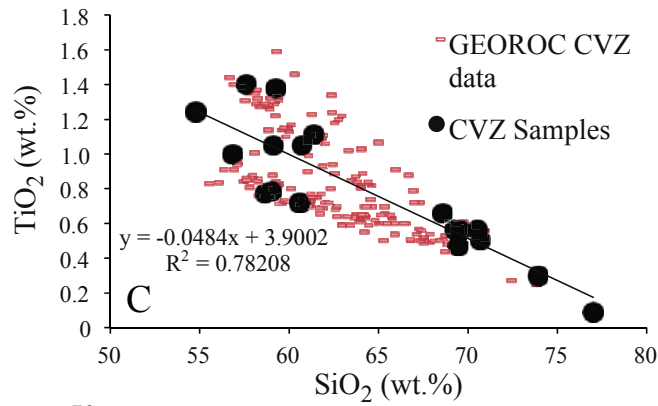
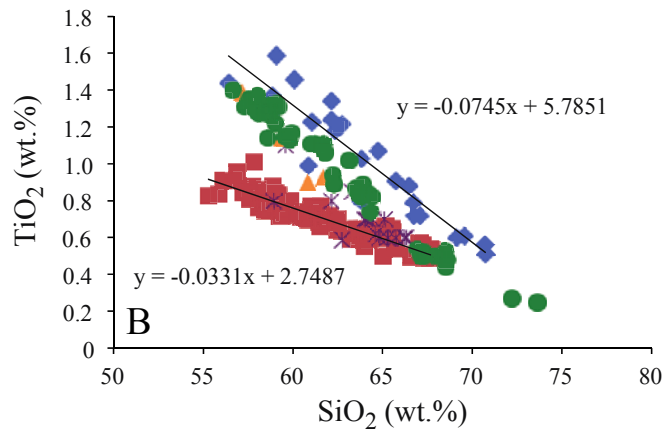
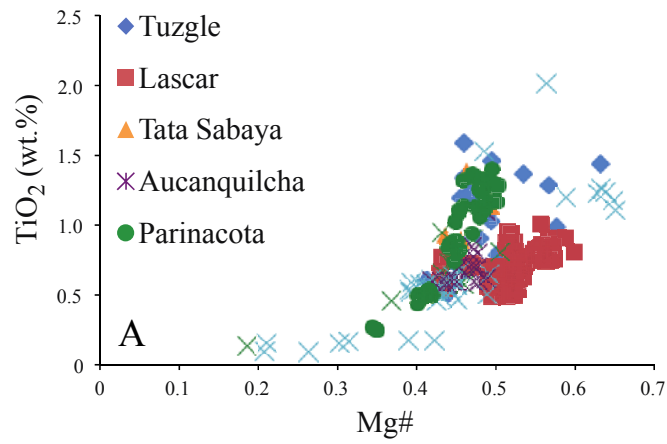


Fig. A.3 All data from GEOROC for various volcanic centers from the CVZ. A) TiO₂ versus Mg# and B) TiO₂ versus SiO₂ (wt.%) with upper regression line through Tuzgöle data, and lower regression line through Lascar data. C) TiO₂ versus SiO₂ (wt.%) and D) La versus SiO₂ (wt.%) with all GEOROC data included in panels A and B as red data points, and samples from our manuscript, overlain as black circles. Panels A and B indicate that LLDs at most CVZ volcanoes show remarkably little scatter despite the pervasive influence of AFC, and among the volcanoes considered in this study, the LLDs are extremely similar. The LLDs are much more distinct and show less scatter using SiO₂ as an index of differentiation when compared to Mg#, suggesting that SiO₂ is the preferred index of differentiation for the CVZ magmatic systems. In the case of major, minor and trace element variations with SiO₂, the single samples from individual volcanoes capture the same relationships as those defined by all samples from all volcanoes.

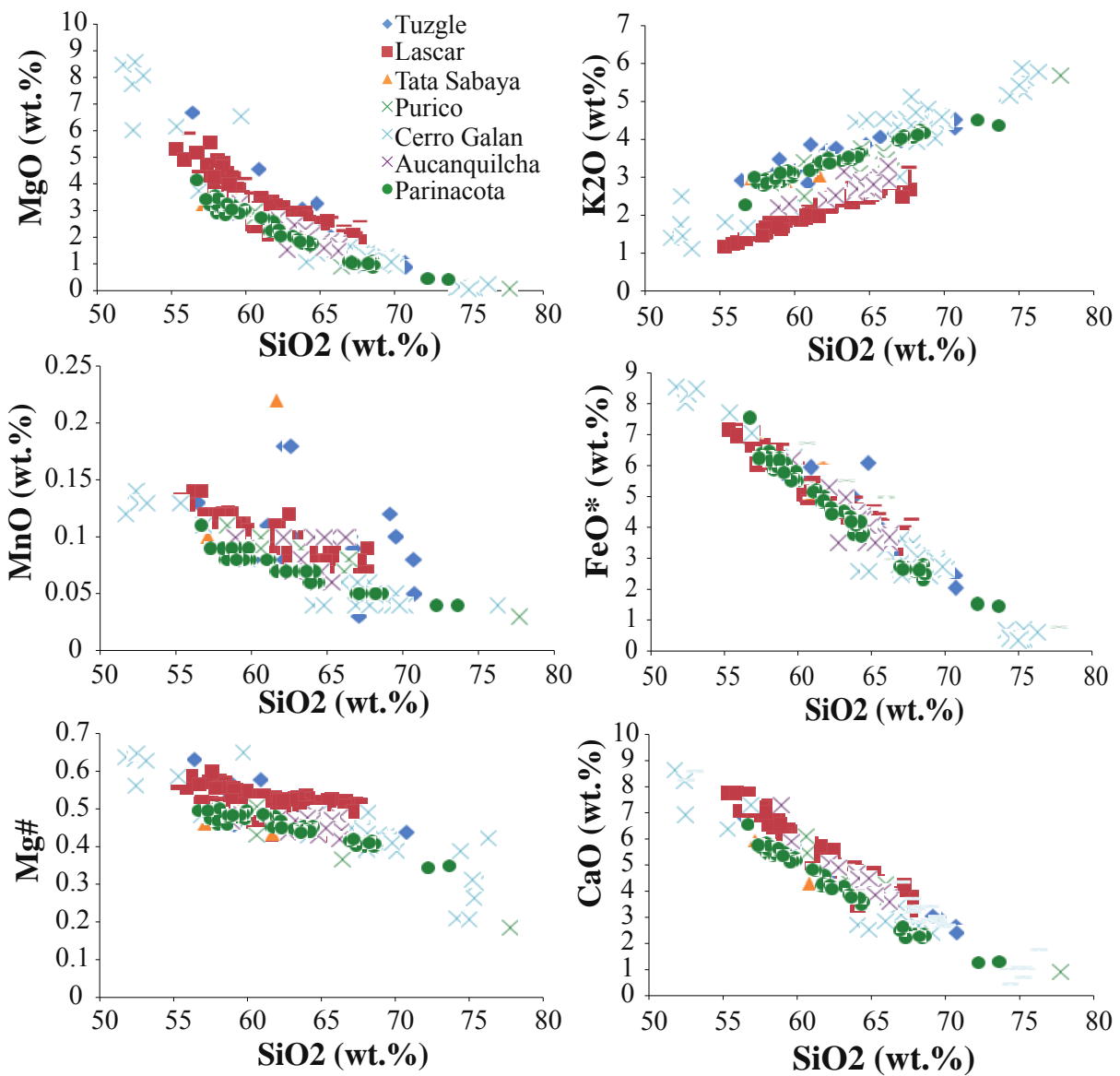


Fig. A.4 Harker Diagrams of GEOROC data for multiple volcanic systems from the CVZ. All panels indicate that LLDs at CVZ volcanoes show remarkably little scatter despite the pervasive influence of AFC, and among the volcanoes considered in this study, the LLDs are extremely similar.

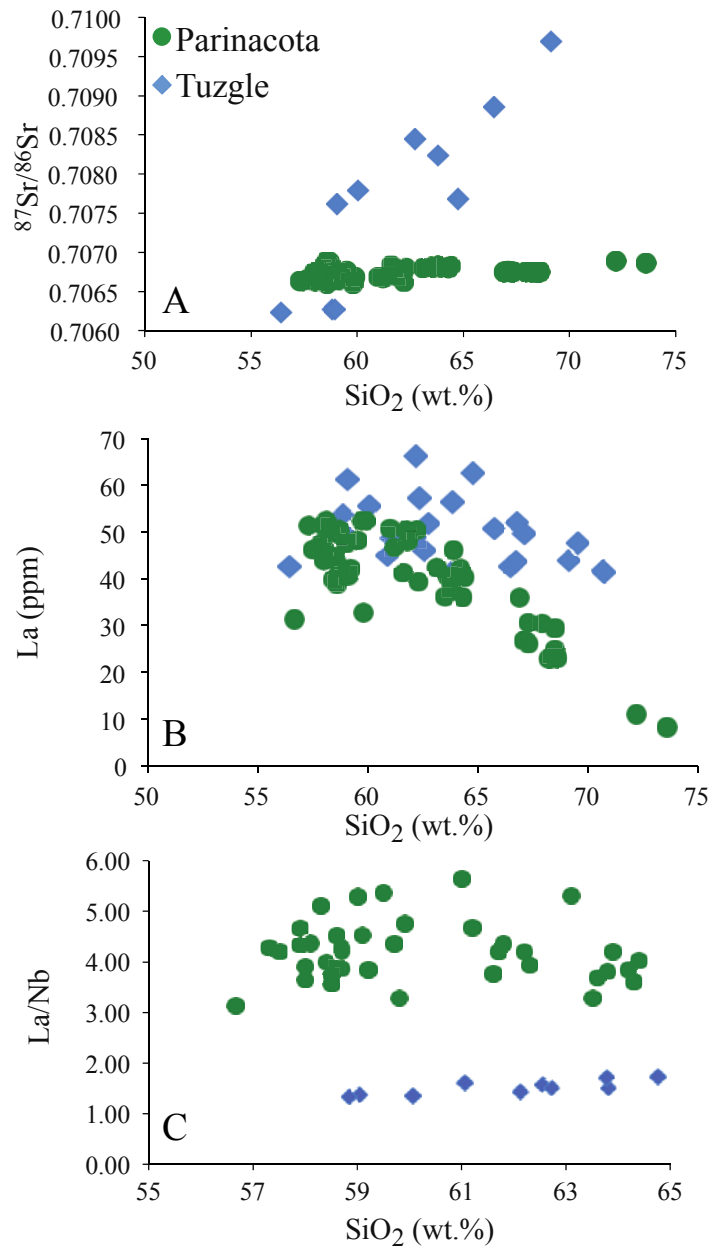


Fig. A.5 Data from GEOROC for Parinacota and Tuzgle volcanoes. A) ⁸⁷Sr/⁸⁶Sr isotopic ratios, B) La versus SiO₂ (wt.%), and C) La/Nb versus SiO₂ (wt.%). The lack of correlation between ⁸⁷Sr/⁸⁶Sr and SiO₂ in the Parinacota magmas suggests that the magmatic system was closed to AFC, whereas the correlation between ⁸⁷Sr/⁸⁶Sr and SiO₂ in Tuzgle magmas indicates the influence of crustal assimilation on the Tuzgle volcanic system. Panel B shows a correlation between La and SiO₂ in the Parinacota magmas, which experienced closed system crystal fractionation, and a lack of correlation between La and SiO₂ in the Tuzgle magmas, which have experienced AFC. Despite these differences, Panel C shows that La/Nb ratios in these two systems remain constant and distinct within each volcano across variations in SiO₂, highlighting the value of trace element ratios over individual trace element concentrations to compare magmatic systems, and the utility of the La/Nb ratio as a proxy for mantle source composition in the CVZ.

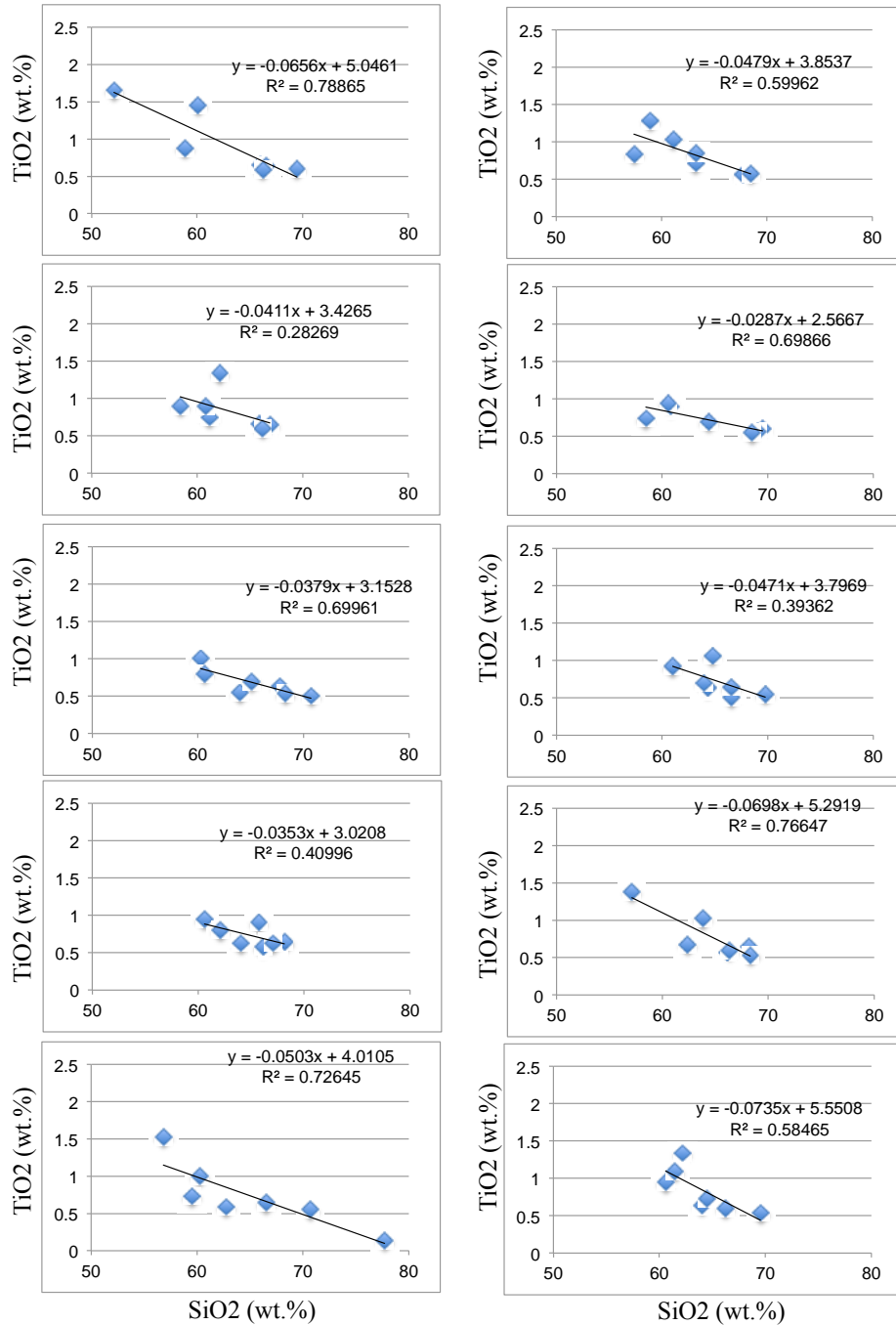


Fig. A.6 Results from a statistical test in which we assigned each sample in the GEOROC data set from a volcano a random number using the random number generator function in MS Excel, and selected the lowest number of a random sample from each volcano. Plots show the TiO₂ versus SiO₂ concentration pairs for each randomly selected sample from each volcano as a group. We performed this exercise ten times. The random samples define linear trends similar to the trend we observe in the compiled CVZ data (see Panel B in Fig A.3).

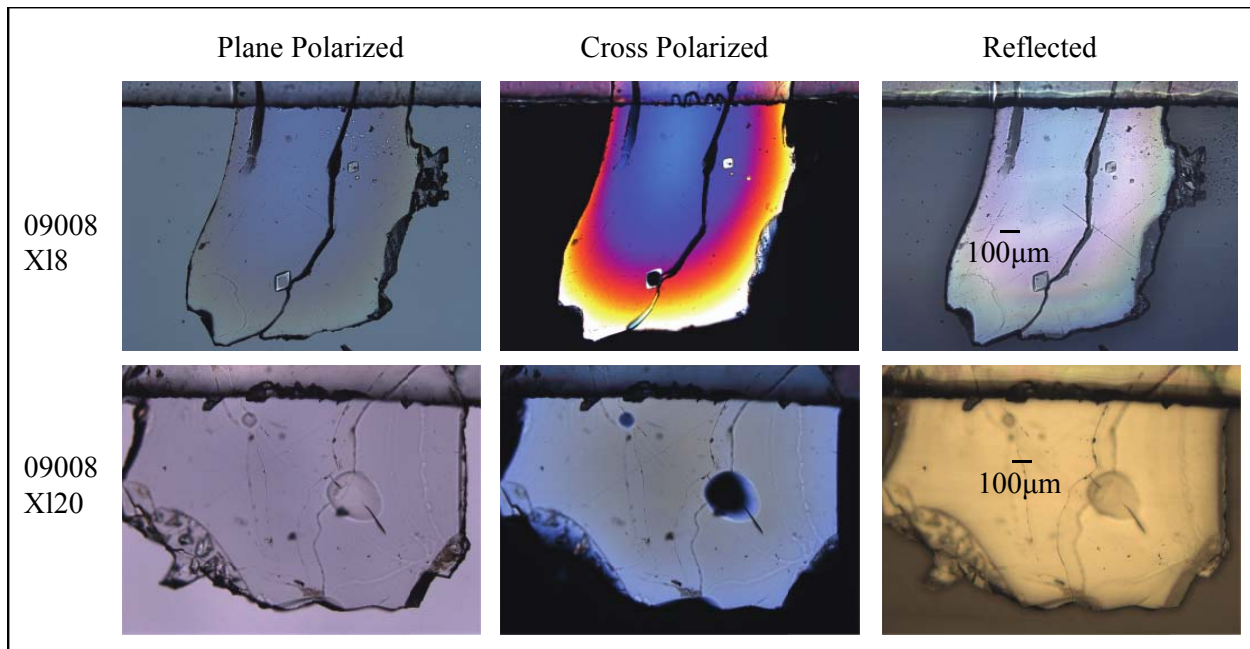


Fig. A.7 Photomicrographs of melt inclusions hosted in Tara plinian fall pumice (sample 09008) erupted from the Guacha Caldera. Scale bars included in reflected images are same for all images.

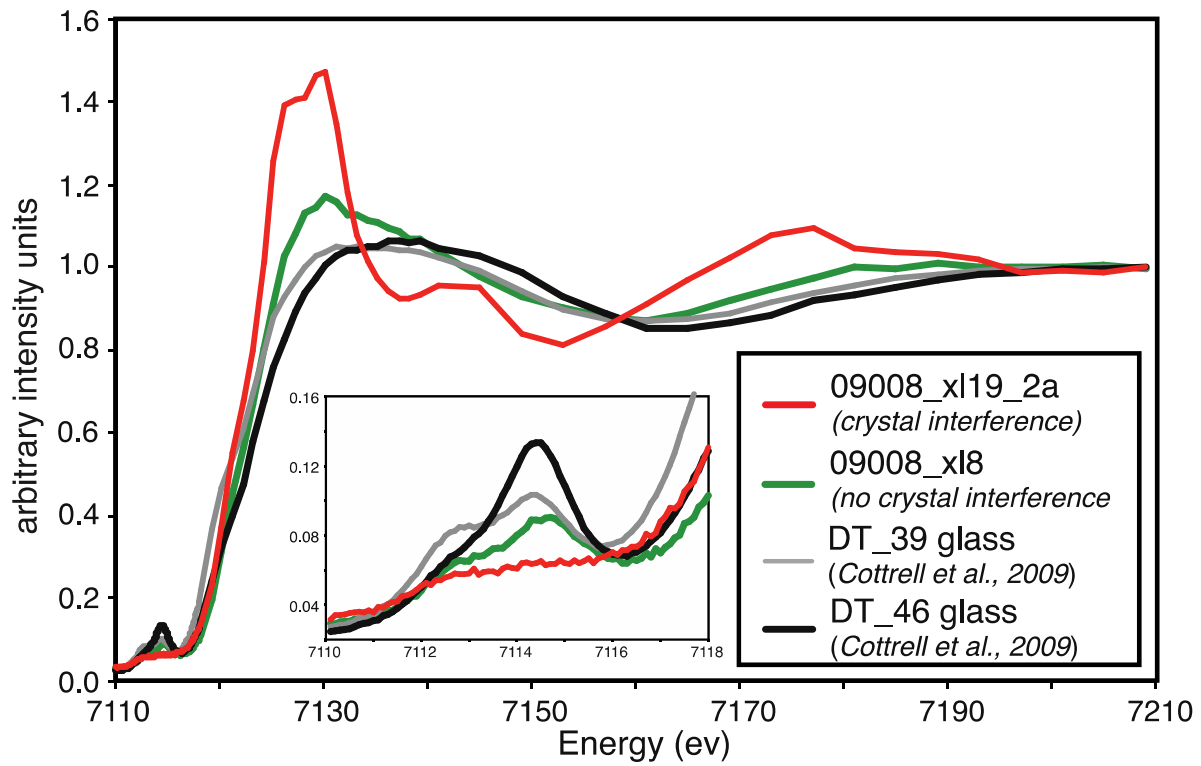


Fig. A.8 Plot of energy vs. intensity for edge-step normalized, baseline-subtracted Fe-K edge XANES fluorescence spectra. Example Fe- μ -XANES spectra for two Tara plinian melt inclusions, erupted from the Guacha caldera (sample 09008_xl19_MI2, red line, crystal interference; melt inclusion sample 09008_xl8, green line, no crystal interference; rhyolite standard glasses from Cottrell et al., (2009). Inset shows a magnified view of the pre-edge for all spectra.

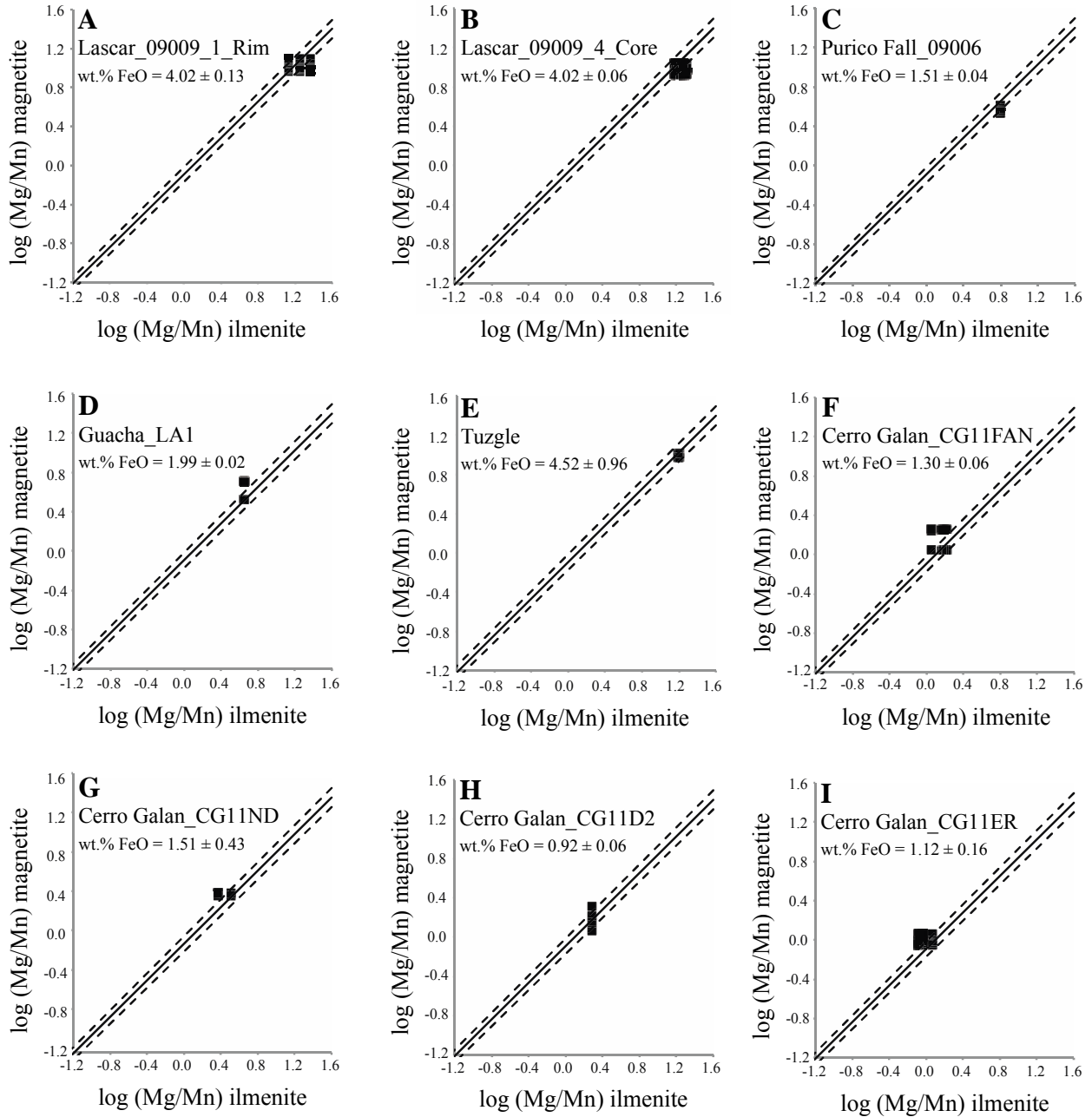


Fig A.9 Plots of $\log (X_{\text{Mg}}/X_{\text{Mn}})_{\text{magnetite}}$ versus $\log (X_{\text{Mg}}/X_{\text{Mn}})_{\text{ilmenite}}$ for all possible pairings of ilmenite and titanomagnetite in each sample. The dashes lines outline the $\pm 2\sigma$ distribution for the data set determined by Bacon and Hirschmann (1988). The average FeO $\pm 2\sigma$ in the melt for the entire Fe-Ti oxide data set is shown for each sample.

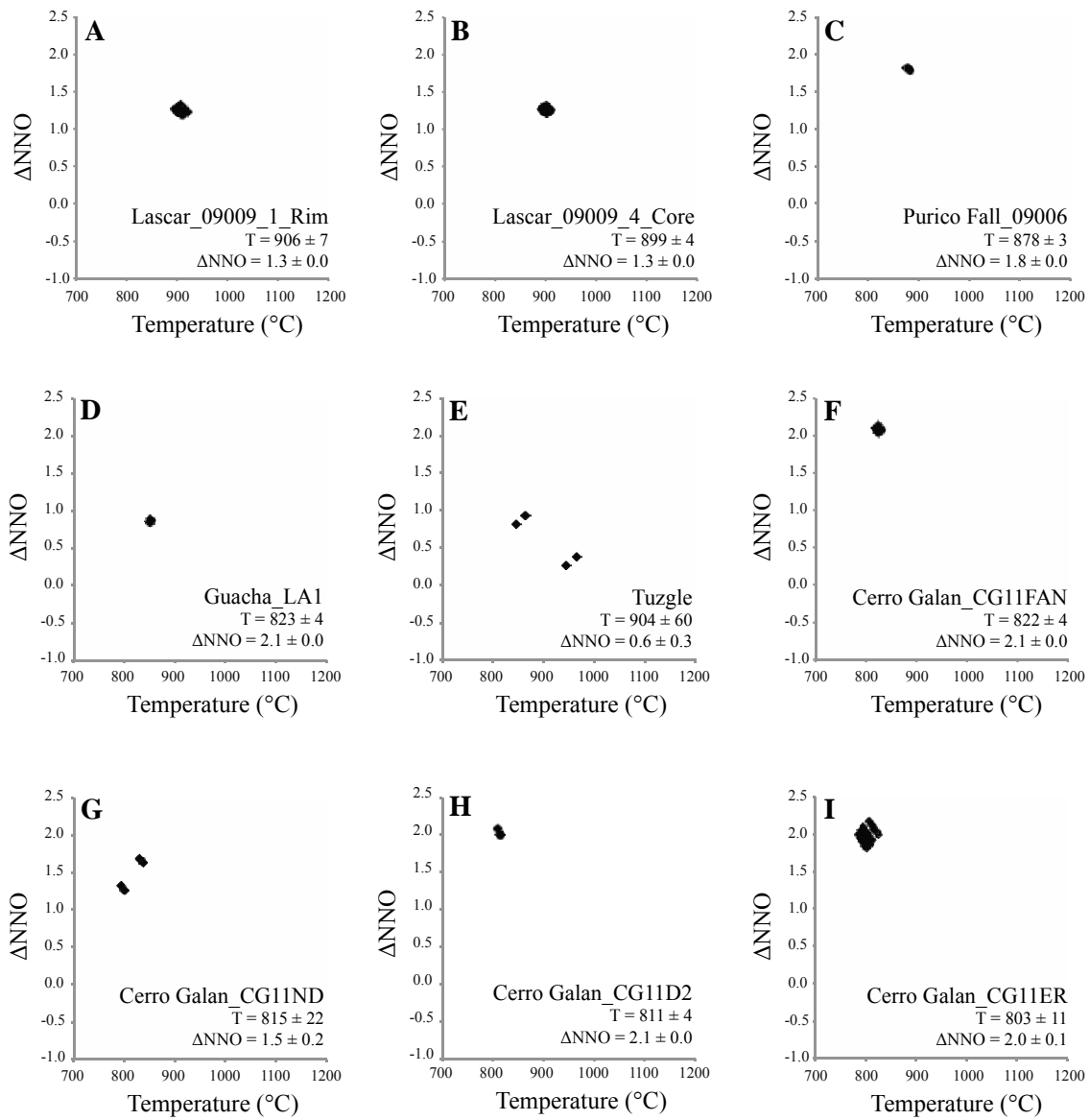


Fig. A.10 Plots of ΔNNO versus temperature calculated for all pairings of ilmenite and titanomagnetite in each sample using the Fe-Ti two oxide model of Andersen and Lindsley (1988). The average ΔNNO and T ($^{\circ}\text{C}$) for all pairings ($\pm 2\sigma$) are given for each sample.

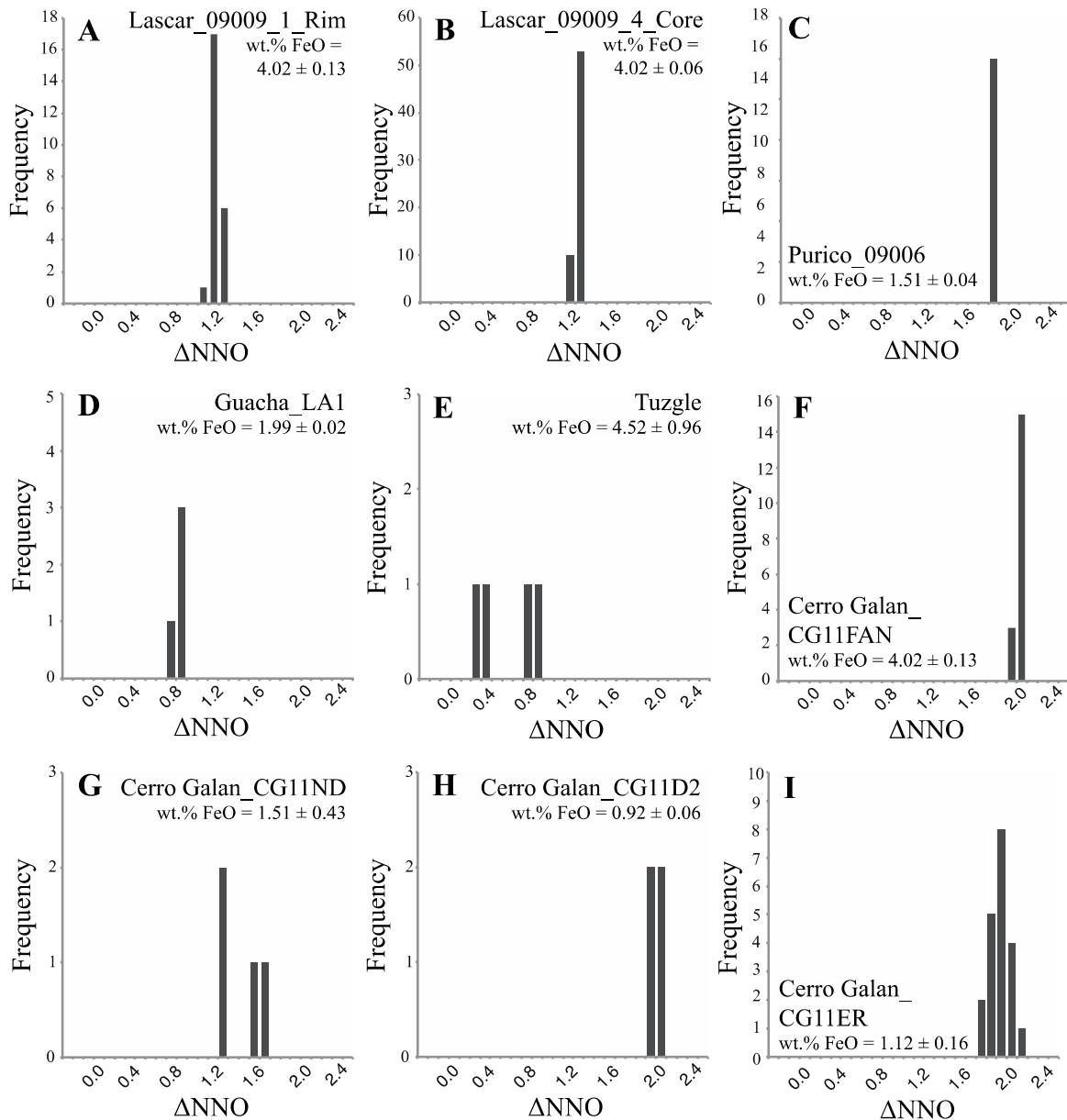


Fig. A.11 Histograms for ΔNNO for all pairings of ilmenite and titanomagnetite in each sample using the Fe-Ti two oxide model of Anderson and Lindsley (1988). Corresponding wt.% FeO values calculating from the model of Kress and Carmichael (1991) are superimposed. The results show there are little variations in wt.% FeO over the full range of all ΔNNO values in each sample.

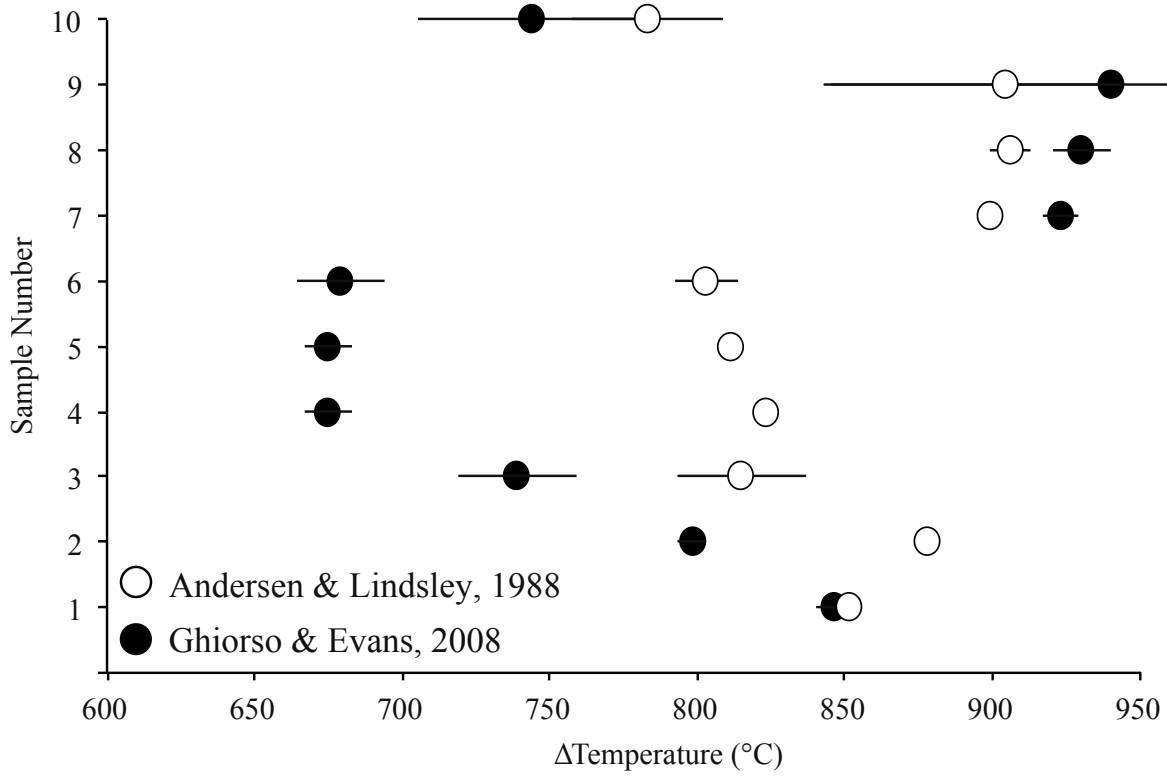


Fig. A.12 Temperature from Fe-Ti oxides in CVZ samples, calculated using the geothermometers of Andersen and Lindsley (1988) and Ghiorso and Evans (2008). Samples analyzed for Fe-Ti oxides listed from 1-10 (1: LA1; 2: 09006; 3:CG11ND; 4:CG11FAN; 5:CG11D2; 6:CG11ER; 7:09009_4; 8:09009_1; 8:Tuzgle; 9:AP0736) and their corresponding temperature derived from the two formulations. At high temperatures the two thermometers show good agreement, however, at low temperatures, the Ghiorso and Evans (2008) formulation extends to very low temperatures that deviate from the values derived from Andersen and Lindsley (1988).

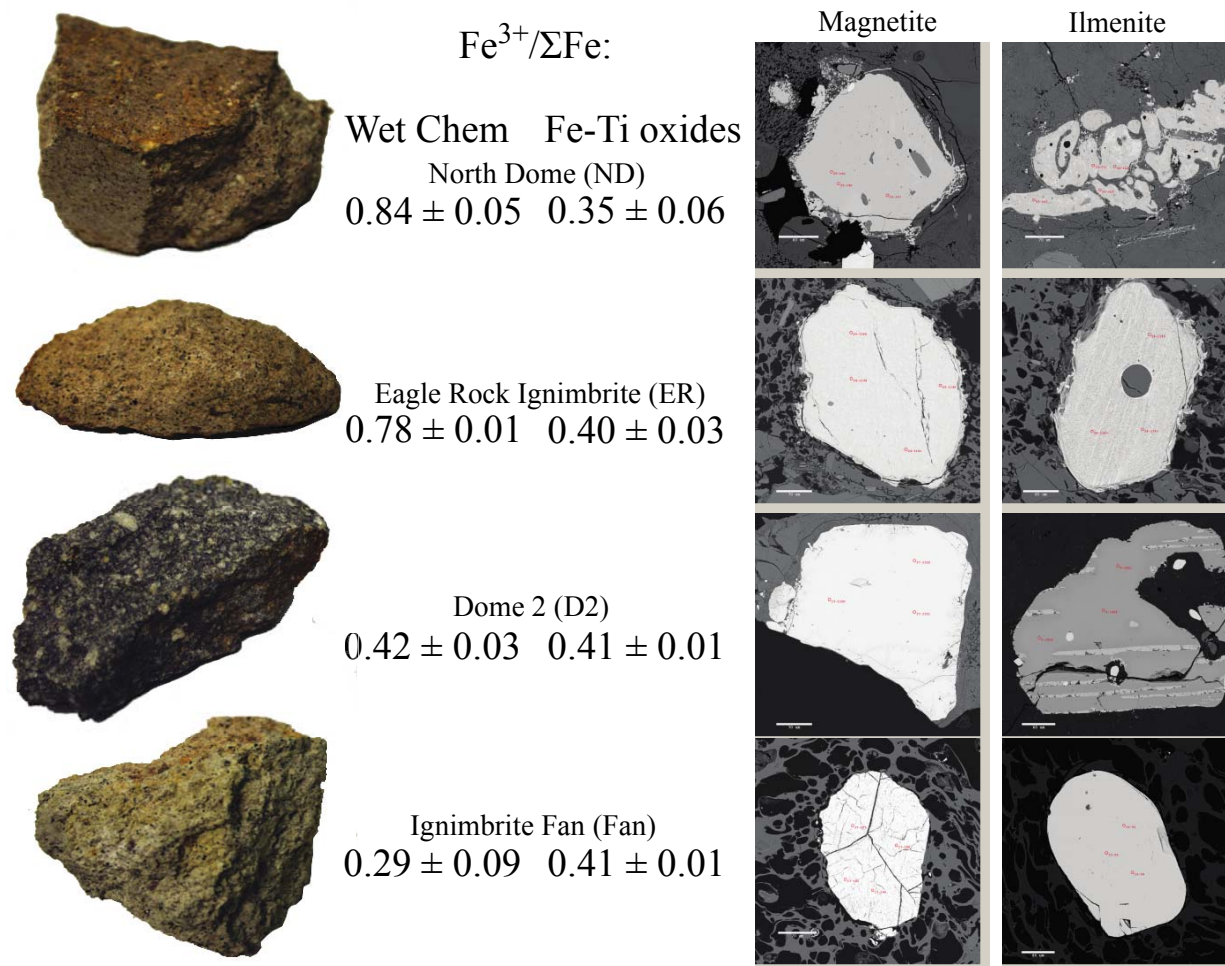


Fig. A.13 Photographs and BSE images of Cerro Galan post-collapse samples. $\text{Fe}^{3+}/\Sigma\text{Fe}$ ratios are included from wet chemistry and oxybarometry. Fe-Ti oxide values are based on averages of all pairings of ilmenite and titanomagnetite (see text) and $\text{Fe}^{3+}/\Sigma\text{Fe}$ ratios are calculated from $f\text{O}_2$ using Kress and Carmichael (1991). Note the varying types of deposits (ignimbrites versus dome samples) and the variation in colors of each sample that imply varying degrees of post-eruptive alteration. For example, although ND and D2 are both lavas, D2 is black in color due to a glassy groundmass and gives a $\text{Fe}^{3+}/\Sigma\text{Fe}$ ratio that is consistent between bulk rock and Fe-Ti oxides. This is in contrast to ND, which is also a lava, yet shows a reddish/orange color and exhibits a high $\text{Fe}^{3+}/\Sigma\text{Fe}$ ratio from bulk rock, wet chemical analysis compared to the $\text{Fe}^{3+}/\Sigma\text{Fe}$ ratio derived from Fe-Ti oxides. Error for each analysis is 1σ .

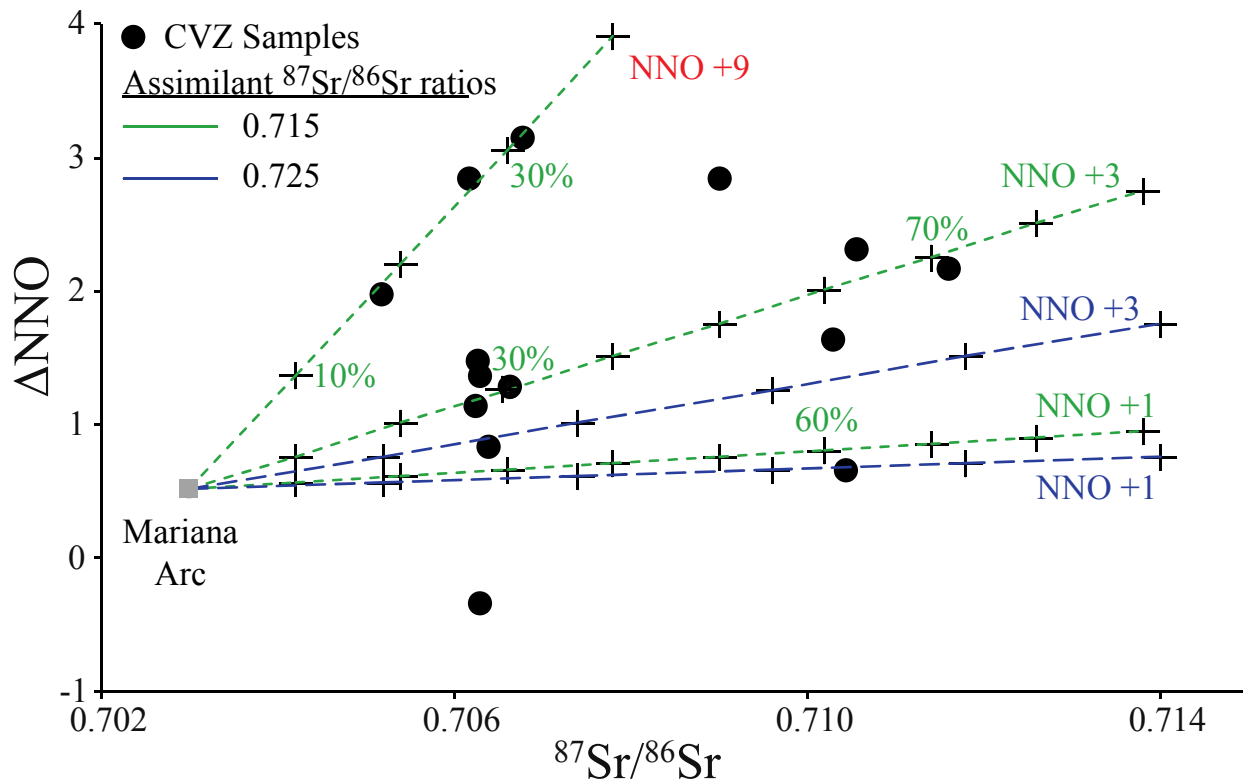


Fig. A.14 Model calculations showing mixing between Mariana arc basaltic melt inclusions and various assimilant compositions at 10% increments.

References

- Andersen, D.J., Lindsley, D.H., 1988. Internally consistent solution models for Fe-Mg-Mn-Ti oxides: Fe-Ti oxides. *Am Mineral.* 73, 714–726.
- Bacon, C.R., Hirschmann, M.M., 1988. Mg/Mn partitioning as test for equilibrium between coexisting Fe-Ti oxides[in volcanic rocks]. *Am Mineral.* 73, 57–61.
- Beck, S.L., Zandt, G., Myers, S.C., Wallace, T.C., Silver, P.G., Drake, L., 1996. Crustal-thickness variations in the central Andes. *Geology.* 24, 407. doi:10.1130/0091-7613(1996)024<0407:CTVITC>2.3.CO;2
- Blundy, J., Cashman, K. and Humphreys, M., 2006. Magma heating by decompression-driven crystallization beneath andesite volcanoes. *Nature*, 443(7107), 76-80.
- Botcharnikov, R.E., Koepke, J., Holtz, F., McCammon, C. and Wilke, M., 2005. The effect of water activity on the oxidation and structural state of Fe in a ferro-basaltic melt. *Geochim Cosmochim Ac.*, 69(21), 5071-5085.
- Brounce, M.N., Kelley, K.A., Cottrell, E., 2014. Variations in $Fe^{3+}/\sum Fe$ of Mariana Arc Basalts and Mantle Wedge fO_2 . *J Petrol.* 55, 2513–2536. doi:10.1093/petrology/egu065
- Burgisser, A., Alletti, M., Scaillet, B., 2015. Simulating the behavior of volatiles belonging to the C–O–H–S system in silicate melts under magmatic conditions with the software D-Compress. *Comput Geosci.* 79, 1-14.
- Candela, P.A., 1986. The evolution of aqueous vapor from silicate melts: effect on oxygen fugacity. *Geochim Cosmochim Ac.*, 50(6), 1205-1211.

- Carmichael, I.S.E., 2014. Chemical Analysis of Silicate Rocks: A Manual. EarthChem Library 1–49.
- Coira, B., Kay, S.M., 1993. Implications of Quaternary volcanism at Cerro Tuzgle for crustal and mantle evolution of the Puna Plateau, Central Andes, Argentina. *Contrib Mineral Petr.* 113, 40–58.
- Cottrell, E., Kelley, K.A., 2011. The oxidation state of Fe in MORB glasses and the oxygen fugacity of the upper mantle. *Earth Planet Sc Lett.* 305, 270–282.
- Cottrell, E., Kelley, K.A., Lanzirotti, A., Fischer, R.A., 2009. High-precision determination of iron oxidation state in silicate glasses using XANES. *Chem Geol.* 268, 167–179. doi:10.1016/j.chemgeo.2009.08.008
- Crabtree, S.M., Lange, R.A., 2012. An evaluation of the effect of degassing on the oxidation state of hydrous andesite and dacite magmas: a comparison of pre- and post-eruptive Fe²⁺ concentrations. *Contrib Mineral Petr.* 163, 209–224. doi:10.1007/s00410-011-0667-7
- Davidson, J.P., de Silva, S.L., 1995. Late Cenozoic magmatism of the Bolivian Altiplano. *Contrib Mineral Petr.* 119, 387–408. doi:10.1007/BF00286937
- Davidson, J.P., Harmon, R.S., Worner, G., 1991. The source of central Andean magmas; Some considerations. *Geol S Am S.* 265, 233–243. doi:10.1130/SPE265-p233
- Davidson, J.P., McMillan N.J., Moorbath, S., Wörner, G., Harmon, R.S., Lopez-Escobar, L., 1990. The Nevados de Payachata volcanic region (18 S/69 W, N. Chile) II. Evidence for widespread crustal involvement in Andean magmatism. *Contrib to Min and Petrol.* 105(4), 412-432.
- de Silva, S., 1989. Geochronology and stratigraphy of the ignimbrites from the 21°30'S to 23°30'S portion of the central Andes of northern Chile. *J Volcanol Geotherm Res.* 37, 93–131. doi:10.1016/0377-0273(89)90065-6
- de Silva, S.L., Davidson, J.P., Croudace, I.W., Escobar, A., 1993. Volcanological and petrological evolution of volcan Tata Sabaya, SW Bolivia. *J Volcanol Geotherm Res.* 55, 305–335. doi:10.1016/0377-0273(93)90043-Q
- de Silva, S., Gosnold, W., 2007. Episodic construction of batholiths: Insights from the spatiotemporal development of an ignimbrite flare-up. *J Volcanol Geotherm Res.* 167, 320–335.
- de Silva, S.L., Zandt, G., Trumbull, R., Viramonte, J.G., Salas, G., Jiménez, N., 2006. Large ignimbrite eruptions and volcano-tectonic depressions in the Central Andes: a thermomechanical perspective, in: Troise, C., de Natale, G., Kilburn, C.R.J. (Eds.), *Mechanisms of Activity and Unrest at Large Calderas*. Geol Soc. London, Special Publications 269, 47-63. doi:10.1144/GSL.SP.2006.269.01.04
- Devine, J.D., Rutherford, M.J., Norton, G.E. and Young, S.R., 2003. Magma storage region processes inferred from geochemistry of Fe–Ti oxides in andesitic magma, Soufriere Hills Volcano, Montserrat, WI. *J Petrol.* 44(8), 1375-1400.
- Deruelle, B., Figueroa, O.A., Medina, E.T., Viramonte, J.G., Maragano, M.C., 1996. Petrology of pumices of April 1993 eruption of Lascar (Atacama, Chile). *Terra Nova* 8(2), 191-199.
- Elliott, T., Plank, T., Zindler, A., White, W. and Bourdon, B., 1997. Element transport from slab to volcanic front at the Mariana arc. *Journal of Geophysical Research: Solid Earth* (1978–2012), 102(B7), 14991-15019.
- Folkes, C.B., de Silva, S.L., Bindeman, I.N., Cas, R.A.F., 2013. Tectonic and climate history influence the geochemistry of large-volume silicic magmas: New $\delta^{18}\text{O}$ data from the Central Andes with comparison to N America and Kamchatka. *J Volcanol Geotherm Res.* 262, 1–16.

doi:10.1016/j.jvolgeores.2013.05.014

- Folkes, C.B., de Silva, S.L., Wright, H.M., Cas, R.A., 2011. Geochemical homogeneity of a long-lived, large silicic system; evidence from the Cerro Galan caldera, NW Argentina. *B Volcanol.* 73, 1455–1486.
- Francis, P.W., Roobol, M.J., Walker, G.P.L., 1974. The San Pedro and San Pablo volcanoes of northern Chile and their hot avalanche deposits. *International J of Earth Sci.* 63, 357–388.
- Frost, B. R., Ballhaus, C., 1998. Comment on "Constraints on the origin of the oxidation state of mantle overlying subduction zones: an example from Simcoe, Washington, USA" by AD Brandon and DS Draper. *Geochim Cosmochim Ac.*, 62, 329-332.
- Gaillard, F., Scaillet, B., Pichavant, M. and Bény, J.M., 2001. The effect of water and fO_2 on the ferric–ferrous ratio of silicic melts. *Chemical Geology*, 174(1), 255-273.
- Gaillard, F., Scaillet, B., Pichavant, M., 2002. Kinetics of iron oxidation-reduction in hydrous silicic melts. *Am Mineral.* 87, 829-837.
- Gaillard, F., Pichavant, M., Mackwell, S., Champallier, R., Scaillet, B. and Mccammon, C., 2003a. Chemical transfer during redox exchanges between H_2 and Fe-bearing silicate melts. *American Mineralogist*, 88(2-3), 308-315.
- Gaillard, F., Schmidt, B., Mackwell, S. and McCammon, C., 2003b. Rate of hydrogen–iron redox exchange in silicate melts and glasses. *Geochimica et Cosmochimica Acta*, 67(13), 2427-2441.
- Gardeweg, M.C., Sparks, R.S.J., Matthews, N.E., 1998. Evolution of Lascar Volcano, Northern Chile. *J Geol Soc London* 155, 89–104. doi:10.1144/gsjgs.155.1.0089
- Ghiorso, M.S., Evans, B.W., 2008. Thermodynamics of Rhombohedral Oxide Solid Solutions and a Revision of the Fe-Ti Two-Oxide Geothermometer and Oxygen-Barometer. *Am J Sci.* 308, 957–1039. doi:10.2475/09.2008.01
- Grove, T.L., Elkins-Tanton, L.T., Parman, S.W., Chatterjee, N., Müntener, O. and Gaetani, G.A., 2003. Fractional crystallization and mantle-melting controls on calc-alkaline differentiation trends. *Contrib Mineral Petr.* 145(5), 515-533.
- Hildreth, W., Moorbath, S., 1988. Crustal Contributions to Arc Magmatism in the Andes of Central Chile - Comment. *Contrib Mineral Petr.* 108, 247–252.
- Humphreys, M.C.S., Brooker, R.A., Fraser, D.G., Burgisser, A., Mangan, M. T., McCammon, C., 2015. Coupled Interactions between Volatile Activity and Fe Oxidation State during Arc Crustal Processes. *J Petrol.* 56(4), 795-814.
- Johnson, D., Hooper, P., Conrey, R., 1999. XRF analysis of rocks and minerals for major and trace elements on a single low dilution Li-tetraborate fused bead. *Advances X-ray Analy* 41, 843–867.
- Jugo, P.J., Wilke, M. and Botcharnikov, R.E., 2010. Sulfur K-edge XANES analysis of natural and synthetic basaltic glasses: Implications for S speciation and S content as function of oxygen fugacity. *Geochim Cosmochim Ac.*, 74(20), 5926-5938.
- Kay, S.M., Coira, B.L., Caffè, P.J., Chen, C.H., 2010. Regional chemical diversity, crustal and mantle sources and evolution of central Andean Puna plateau ignimbrites. *J Volcanol Geotherm Res.* 198, 81–111.
- Kay, S.M., Coira, B., Worner, G., Kay, R.W., Singer, B.S., 2011. Geochemical, isotopic and single crystal $^{40}Ar/^{39}Ar$ age constraints on the evolution of the Cerro Galán ignimbrites. *B Volcanol.* 73, 1487–1511.
- Kelley, K.A., Cottrell, E., 2009. Water and the Oxidation State of Subduction Zone Magmas. *Science* 325, 605–607. doi:10.1126/science.1174156

- Kelley, K.A., Cottrell, E., 2012. The influence of magmatic differentiation on the oxidation state of Fe in a basaltic arc magma. *Earth Planet Sc Lett.* 329-330, 109–121.
doi:10.1016/j.epsl.2012.02.010
- Klerkx, J., Deutsch, S., Pichler, H., Zeil, W., 1977. Strontium isotopic composition and trace element data bearing on the origin of Cenozoic volcanic rocks of the central and southern Andes. *J Volcanol Geotherm Res* 2, 49–71.
- Kress, V.C., Carmichael, I., 1991. The compressibility of silicate liquids containing Fe₂O₃ and the effect of composition, temperature, oxygen fugacity and pressure on their redox state. *Contrib Mineral Petr.* 108, 82–92.
- Lindsay, J., Schmitt, A., Trumbull, R., de Silva, S., Siebel, W., Emmermann, R., 2001. Magmatic evolution of the La Pacana caldera system, Central Andes, Chile: Compositional variation of two cogenetic, large-volume felsic ignimbrites. *J Petrol.* 42, 459–486.
- Lucassen, F., Becchio, R., Wilke, H.G., Franz, G., Thirlwall, M.F., Viramonte, J., Wemmer, K., 2000. Proterozoic–Paleozoic development of the basement of the Central Andes (18–26°S) — a mobile belt of the South American craton. *Journal of South American Earth Sciences* 13, 697–715.
- Lucassen, F., Becchio, R., Harmon, R., Kasemann, S., Franz, G., Trumbull, R., Wilke, H.-G., Romer, R.L., Dulski, P., 2001. Composition and density model of the continental crust at an active continental margin—the Central Andes between 21 and 27 S. *Tectonophysics* 341, 195–223.
- Matthews, S.J., Jones, A.P., Beard, A.D., 1994. Buffering of melt oxygen fugacity by sulphur redox reactions in calc-alkaline magmas. *Journal of the Geol. Soc.*, 151(5), 815–823.
- Matthews, S.J., Sparks, R.S.J., Gardeweg, M.C., 1999. The Piedras Grandes–Soncor Eruptions, Lascar Volcano, Chile; Evolution of a Zoned Magma Chamber in the Central Andean Upper Crust. *J Petrol.* 40, 1891–1919. doi:10.1093/petroj/40.12.1891
- Moore, G., Richter, K. and Carmichael, I.S.E., 1995. The effect of dissolved water on the oxidation state of iron in natural silicate liquids. *Contrib Mineral Petr.*, 120(2), 170–179.
- Mungall, J.E., 2002. Roasting the mantle: slab melting and the genesis of major Au and Au-rich Cu deposits. *Geology*, 30(10), 915–918.
- Norabuena, E.O., Dixon, T.H., Stein, S. and Harrison, C.G., 1999. Decelerating Nazca-South America and Nazca-Pacific plate motions. *Geophys Res Lett.* 26(22), 3405–3408.
- Ort, M.H., Coira, B.L., Mazzoni, M.M., 1996. Generation of a crust-mantle magma mixture: magma sources and contamination at Cerro Panizos, central Andes. *Contrib Mineral Petr.* 123, 308–322.
- Pallister, J.S., Hoblitt, R.P., Meeker, G.P., Knight, R.J. and Siems, D.F., 1996. Magma mixing at Mount Pinatubo: petrographic and chemical evidence from the 1991 deposits. In: *Fire and mud: eruptions and lahars of Mount Pinatubo, Philippines*, 687–731.
- Ramos, F.C., 1992. *Isotope Geology of the Metamorphic Core of the Central Grouse Creek Mountains, Box Elder County, Utah.* University of California Los Angeles.
- Ramos, V.A., Jordan, T.E., Allmendinger, R.W., Mpodozis, C., Kay, S.M., Cortés, J.M., Palma, M., 1986. Paleozoic terranes of the central Argentine - Chilean Andes. *Tectonics* 5, 855–880.
- Salisbury, M., Jicha, B., de Silva, S., Singer, B., Jimenez, C., Ort, M., 2011. ⁴⁰Ar/³⁹Ar chronostratigraphy of Altiplano-Puna Volcanic Complex ignimbrites reveals the development of a major magmatic province. *Geol Soc Am Bull.* 123, 821–840.
- Scaillet, B., Evans, B.W., 1999. The 15 June 1991 eruption of Mount Pinatubo. I. Phase

- equilibria and pre-eruption P - T - fO_2 - fH_2O conditions of the dacite magma. *J Petrol.* 40(3), 381-411.
- Schmitt, A., de Silva, S.L., Trumbull, R., Emmermann, R., 2001. Magma evolution in the Purico ignimbrite complex, northern Chile: evidence for zoning of a dacitic magma by injection of rhyolitic melts following mafic recharge. *Contrib Mineral Petr.* 140, 680–700.
doi:10.1007/s004100000214
- Soler, M.M., Caffè, P.J., Coira, B.L., Onoe, A.T., Kay, S.M., 2007. Geology of the Vilama caldera: A new interpretation of a large-scale explosive event in the Central Andean plateau during the Upper Miocene. *J Volcanol Geotherm Res.* 164, 27–53.
- Straub, S.M., Gómez-Tuena, A., Zellmer, G.F., Espinasa-Perena, R., Stuart, F.M., Cai, Y., Langmuir, C.H., Martin-Del Pozzo, A.L., Mesko, G.T., 2013. The processes of melt differentiation in arc volcanic rocks: Insights from OIB-type arc magmas in the central Mexican volcanic belt. *J Petrol.* 54(4) 665-701.
- Syracuse, E.M., Abers, G.A., 2006. Global compilation of variations in slab depth beneath arc volcanoes and implications. *Geochem Geophys Geosy.* 7(5) 1-18.
doi:10.1029/2005GC001045
- Walker, B.A., Jr., 2011. *The Geochemical Evolution of the Aucanquilcha Volcanic Cluster: Prolonged Magmatism and its Crustal Consequences 1–217*, Oregon State University, Corvallis.
- Walker, B.A., Grunder, A.L., Wooden, J.L., 2010. Organization and thermal maturation of long-lived arc systems: Evidence from zircons at the Aucanquilcha volcanic cluster, northern Chile. *Geology* 38, 1007–1010. doi:10.1130/G31226.1
- Walker, B.A., Klemetti, E.W., Grunder, A.L., Dilles, J.H., Tepley, F.J., Giles, D., 2013. Crystal reaming during the assembly, maturation, and waning of an eleven-million-year crustal magma cycle: thermobarometry of the Aucanquilcha Volcanic Cluster. *Contrib Mineral Petr.* 165, 663–682.
- Wörner, G., Harmon, R.S., Davidson, J., Moorbath, S., Turner, D.L., McMillan, N., Nyes, C., Lopez-Escobar, L. and Moreno, H., 1988. The Nevados de Payachata volcanic region (18 S/69 W, N. Chile). *Bull Volcan.* 50(5), 287-303.